Unified Nusselt- and Sherwood-number correlations in axisymmetric finite-gap stagnation and rotating-disk flows

Michael E. Coltrin [a,*], Robert J. Kee [b]

[a] Sandia National Laboratories, Albuquerque, NM 87185, USA
[b] Department of Mechanical Engineering, Colorado School of Mines, Golden, CO 80401, USA

ABSTRACT

This paper develops a unified analysis of stagnation flow heat and mass transport, considering both semi-infinite domains and finite gaps, with and without rotation of the stagnation surface. An important objective is to derive Nusselt- and Sherwood-number correlations that represent heat and mass transport at the stagnation surface. The approach is based on computationally solving the governing conservation equations in similarity form as a boundary-value problem. The formulation considers ideal gases and incompressible fluids. The correlated results depend on fluid properties in terms of Prandtl, Schmidt, and Damköhler numbers. Heterogeneous chemistry at the stagnation surface is represented as a single first-order reaction. A composite Reynolds number represents the combination of stagnation flows with and without stagnation-surface rotation.

Published by Elsevier Ltd.

1. Introduction

Axisymmetric stagnation flows have the remarkable property that heat- and mass-transfer fluxes to the stagnation surface can be highly uniform. This characteristic is technologically valuable and reactors are designed to exploit the inherent flux uniformity. Implementations of stagnation flows find numerous applications in technology, for example chemical-vapor-deposition (CVD) reactors [1–5] and rotating-disk electrodes [6–8], as well as in laboratory-scale reactors that support fundamental research into reaction chemistry in such areas as materials deposition, electrochemistry, catalysis and combustion [9–21].

The objective of the present paper is to develop general correlations for heat and mass transfer at the stagnation surface. In dimensionless terms, this means developing correlations for the Nusselt and Sherwood numbers in terms of their dependence on the Reynolds, Prandtl, Schmidt, and Damköhler numbers. Achieving such general correlations depends upon significant assumptions and simplifications, including constant properties and single-step chemistry.

The correlated results provide valuable insights and rules of thumb for scaling relationships and expected reactor behavior. For example, knowledge of the heat transfer coefficient (Nusselt number) is useful in reactor design to determine the required

power to a heated stagnation surface as a function of gas flows, pressure, etc. in a deposition system. Understanding of the mass-transfer coefficient (Sherwood number) can provide guidance in operating-parameter trade-offs when optimizing deposited-material quality, which might include temperature or pressure dependence or minimizing parasitic chemistry. Another design consideration might be understanding the effects of actively heating or cooling the reactor inlet manifold on expected growth rate. However, such correlations certainly do not replace more comprehensive computational fluid dynamics (CFD) models for detailed reactor and process design and development [22–25].

1.1. Background

The basic mathematical behavior of stagnation flow were first recognized and reported by Heimenz in 1911 [26]. In 1936, Homann extended Heimenz' planar analysis to include axisymmetric flow [27]. In 1921, von Kármán reported a mathematically analogous flow in the boundary layer above a rotating disk [28]. These early research initiatives were based on physical and mathematical insight and analysis, without the benefit of computational solution. Both the stagnation and rotating-disk flow analyses led to combining the continuity and momentum equations into a single third-order ordinary-differential-equation boundary-value problem. Although these early papers are historically consequential, they are practically inaccessible for many readers. The fundamental theory, derivations, and analyses may be found in more recent

* Corresponding author. Tel.: +1 (505) 844 7843.
  E-mail address: mecoltr@sandia.gov (M.E. Coltrin).

texts and monographs on fluid mechanics and boundary layers [29–31,30,32]. The mathematical and computational development in the present paper follows most closely that reported by Kee et al. [29].

There is a vast literature concerning stagnation flows and rotating-disk flows. Historically, these flows have been recognized as being closely related, but have been modeled as being distinctly different. In fact, as discussed by Kee et al. [29], the stagnation and rotating-disk flows, including the semi-infinite and finite-gap domains, can be represented with a common set of differential equations.

The historical stagnation-flow literature is based upon assuming a semi-infinite environment above the viscous boundary layer near the stagnation surface, where the outer flow behaves as an inviscid potential flow. Although this formulation is appropriate in some settings (e.g., external aerodynamics), it is not generally appropriate for confined-flow applications such as CVD reactors or condensed-phase vessels. As illustrated in Fig. 1, the feed stream may be introduced at a specified flow rate through a manifold a some fixed height above the stagnation surface. This so-called finite-gap setting changes the mathematical characteristics of the boundary-value problem to be solved [29,33–38]. Specifically, the finite-gap formulation requires the introduction of an eigenvalue associated with the radial pressure gradient.

As illustrated by the streamlines in Fig. 1 the velocity field clearly has two-dimensional content. However, as illustrated by the shaded background, the scalar fields (e.g., temperature, composition, and density) depend only on the axial position and are radially independent. Most applications of practical interest involve heat and mass transfer, as well as chemical reactions [35,38,39]. The scalar fields remain radially independent even when homogeneous chemistry is involved. It is the inherent radial independence that enables the desired deposition uniformity in chemical vapor deposition processes.

Fig. 1 shows an inlet manifold and stagnation surface with finite radial dimensions. Of course, any real reactor must have finite dimensions as well as external walls that confine the reactive fluids. However, the present analysis is based on ideal stagnation flow, assuming infinite radial extent of the inlet and the stagnation surface. Fortunately, to a very good approximation, real reactors can be designed and operated in regimes that closely reproduce the ideal flow [40–49].

The following Section presents the governing equations in a general setting and in dimensionless similarity form. As is usually the case, the dimensionless equations depend on characteristic length and velocity scales. The present formulation choses four sets of characteristic scales to represent the semi-infinite and finite-gap configurations, with and without stagnation-surface rotation. The Nusselt and Sherwood numbers follow from the computational solution of the dimensionless differential equations. Correlated results are found to depend on a composite Reynolds number that combines rotating-disk and stagnation-flow behavior.
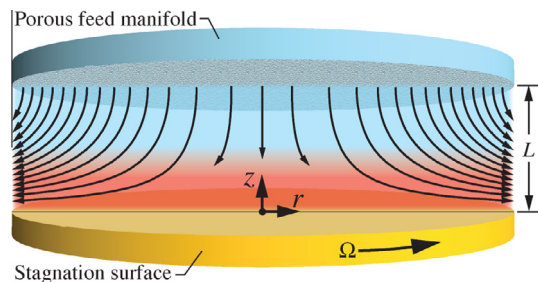

Fig. 1. Illustration of a finite-gap stagnation-flow reactor, where the lower stagnation surface may rotate.

When considering incompressible fluids, the analysis assumes constant properties (conductivity, viscosity, diffusion coefficients, heat capacity). In the case of ideal gases, the Prandtl and Schmidt numbers are presumed to be constants, which is a very good assumption. Because the Prandtl number for gases remains essentially constant there is no specific restriction in the formalism on the temperature dependence of the individual contributing properties. In fact, they may take their usual temperature dependences, with virtually no compromise of the model assumptions.

2. Governing equations

Beginning with the full steady-state axisymmetric Navier–Stokes equations (including thermal and species conservation), Kee, et al. [29] provide detailed derivations of the stagnation-flow equations in boundary-value form. In brief, there are two underlying postulates. First, assume that the streamfunction Ψ can be represented in a separable form as

$$\Psi(z,r) = r^2 U(z),\tag{1}$$

where $U(z)$ is an as-yet unspecified function of z alone. Using the definition of the axisymmetric streamfunction, it follows directly that

$$\frac{\partial \Psi}{\partial r} = \rho u r = 2rU, \quad -\frac{\partial \Psi}{\partial z} = \rho v r = -r^2 \frac{dU}{dz},\tag{2}$$

where ρ is the mass density and u and v are the axial and radial velocities, respectively. Second, assume that temperature and species composition are functions of z alone (cf., Fig. 1). With these assumptions, the axisymmetric Navier–Stokes equations can be transformed to a system of ordinary differential equations. Then, there must be a set of boundary conditions that do not contradict the assumptions. Fortunately, this is the case. For the purposes of the present paper, homogeneous gas-phase chemistry is neglected. Without repeating the derivations, the system of governing equations can be written as:

Mass continuity:

$$\frac{d(\rho u)}{dz} + 2\rho V = 0,\tag{3}$$

Radial momentum:

$$\rho u \frac{dV}{dz} + \rho \left(V^2 - W^2\right) = -\Lambda_r + \frac{d}{dz}\left(\mu \frac{dV}{dz}\right),\tag{4}$$

Circumferential momentum:

$$\rho u \frac{dW}{dz} + 2\rho V W = \frac{d}{dz}\left(\mu \frac{dW}{dz}\right),\tag{5}$$

Thermal energy:

$$\rho u c_p \frac{dT}{dz} = \frac{d}{dz}\left(\lambda \frac{dT}{dz}\right),\tag{6}$$

Species continuity:

$$\rho u \frac{dY}{dz} = \frac{d}{dz}\left(\rho D \frac{dY}{dz}\right),\tag{7}$$

The independent variable z is the height above the stagnation surface. The dependent variables include the axial velocity u and the scaled radial velocity $V = v/r$, where v is the radial velocity and r is the radial coordinate. The scaled circumferential velocity is $W = w/r$, where w is the circumferential velocity. The temperature is represented as T and Y is the mass fraction of a trace species in a chemically inert carrier. In the case of a gas, the pressure p and density ρ are related via the ideal-gas equation of state.

$$p = \rho RT.\tag{8}$$

Fluid properties include the dynamic viscosity μ, thermal conductivity λ, diffusion coefficient D, and heat capacity c_p. The pressure-gradient eigenvalue is defined as

$$\Lambda_r \equiv \frac{1}{r}\frac{dp}{dr}. \tag{9}$$

2.1. Mathematical characteristics

Eqs. (4)–(6) are a system of second-order ordinary differential equations. As such, their solution requires boundary conditions for V, W, Y, and T at both extremities of the z domain. However, Eq. (3) is a first-order equation that requires only one boundary condition for u. In all cases considered here, $u = 0$ at the stagnation surface. In the finite-gap cases (illustrated in Fig. 1), the axial velocity is known at both the inlet manifold ($z = L$) and at the stagnation surface. This apparent over-specification is resolved by evaluating the pressure-gradient Λ_r as an eigenvalue. In the semi-infinite cases, the outer-edge axial velocity cannot be independently specified. Rather, the extent of the z domain must be adjusted so as to be outside the viscous boundary layer and satisfy the outer potential flow.

2.2. Stagnation-surface boundary conditions

Boundary conditions are imposed to specialize the equations to one of four subcases:

- Semi-infinite stagnation flow.
- Finite-gap stagnation flow.
- Semi-infinite rotating disk.
- Finite-gap rotating disk.

Some boundary conditions are common to all the subcases. At the stagnation surface ($z = 0$),

$$u = 0, \quad V = 0, \quad W = \Omega r, \quad T = T_s, \quad D\frac{dY}{dz} = kY_s, \tag{10}$$

where T_s is the stagnation surface temperature and Y_s is the fluid mass fraction at the stagnation surface. The disk rotation rate is specified as Ω. The simplified form of the reaction–diffusion balance is based on a single irreversible reaction that is first-order in the concentration of species A (e.g., A → B). Under these circumstances the surface reaction rate (time-rate-of-change of the mass of species A per unit surface area per unit time $\dot{m}$) is given by

$$\dot{m} = -k[A]W_A = -k\left(\frac{\rho Y_s}{W_A}\right)W_A = -k\rho Y_s, \tag{11}$$

where k is the reaction rate constant ($m\,s^{-1}$), [A] is the molar concentration of the reacting species A ($mol\,m^{-3}$), Y_s is its mass fraction at the surface, and W_A is its molecular weight ($kg\,mol^{-1}$). The axial component of the diffusive mass flux at the surface is

$$j_A = -\rho D\frac{dY}{dz}. \tag{12}$$

The mass balance at the surface requires

$$D\frac{dY}{dz} = kY_s. \tag{13}$$

In the limit that the reaction rate vanishes (i.e., $k = 0$), and without homogeneous chemistry, the mass fraction at the surface must be the same as the inlet, $Y_s = Y_{in}$ and the mass flux at the surface vanishes (i.e., $dY/dz = 0$). In the limit of an infinitely fast reaction, the mass fraction at the surface Y_s must asymptotically approach $Y_s = 0$. However, the reaction rate must obey physical constraints

and cannot be infinite. Considering a gas-surface reaction, the rate constant can be expressed in terms of a sticking coefficient (reaction probability per collision with the surface) as

$$k = \gamma\sqrt{\frac{RT_s}{2\pi W_A}}, \tag{14}$$

where γ is the sticking coefficient, R is the gas constant, and T_s is the surface temperature. Interpreted physically, the reaction can proceed no faster than if every molecule of species A that strikes the surface results in its chemical reaction, or $\gamma = 1$.

2.3. Outer boundary conditions

For the *semi-infinite stagnation flow* case, the outer boundary condition is specified in terms of a potential-flow solution. Outside the viscous boundary layer near the stagnation surface, the outer potential flow can be represented as

$$u = -az, \quad v = \frac{a}{2}r, \quad \frac{1}{r}\frac{dp}{dr} = -\rho\frac{a^2}{4}, \tag{15}$$

where a is the so-called strain-rate parameter [50,29]. Additionally, the outer temperature and composition are specified as $T = T_{in}$ and $Y = Y_{in}$. The extent of the z domain is not known a priori. The domain must be sufficiently large to realize the outer potential flow (i.e., Eq. (15)).

For the *finite-gap stagnation flow* case, the outer boundary conditions are applied at $z = L$. The inlet axial velocity, radial velocity, temperature, and composition are specified as $u = -U_{in}, V = 0, T = T_{in}$, and $Y = Y_{in}$. Notice that the system of equations is first-order in u. However, in the finite-gap case, the value of V is specified on both boundaries. This apparent over-specification is resolved by the radial pressure gradient Λ_r being determined as an eigenvalue.

For the *semi-infinite rotating disk* case, the outer flow is specified simply as a uniform axial velocity with zero radial velocity. The magnitude of the outer axial velocity depends on the disk rotation rate and cannot be specified independently. The outer temperature and composition are specified as $T = T_{in}$ and $Y = Y_{in}$. The extent of the z domain is not known a priori and must be sufficiently large as to extend outside the viscous boundary layer.

For the *finite-gap rotating disk* case, the outer boundary conditions are applied at $z = L$. The inlet axial velocity, radial velocity, temperature, and composition are specified as $u = -U_{in}, V = 0$, $T = T_{in}$, and $Y = Y_{in}$. As noted for the finite-gap stagnation flow case, the system of equations is first-order in u. The radial pressure gradient Λ_r must be determined as an eigenvalue.

2.4. Dimensionless variables

Generalization and correlation of results is greatly facilitated by casting the governing equations in dimensionless form. The dimensionless variables depend on characteristic length $\mathcal{L}$ and velocity $\mathcal{U}$ scales. The dimensionless axial coordinate z and dimensionless velocities are defined as

$$\hat{z} = \frac{z}{\mathcal{L}}, \quad \hat{u} = \frac{u}{\mathcal{U}}, \quad \hat{V} = \frac{\mathcal{L}}{\mathcal{U}}V, \quad \hat{W} = \frac{\mathcal{L}}{\mathcal{U}}W. \tag{16}$$

Table 1 states the characteristic scales for the four subcases being considered. The dimensionless density and pressure are represented as

$$\hat{\rho} = \frac{\rho}{\rho_{in}}, \quad \hat{p} = \frac{p}{\rho_{in}\mathcal{U}^2}, \tag{17}$$

where ρ_{in} is the inlet density. The dimensionless pressure-gradient eigenvalue is

Table 1
Characteristic scales and dimensionless groups.

Geometry	$\mathcal{L}$	$\mathcal{U}$	Re	$\hat{\Lambda}_r$
Semi-infinite, without rotation	$\sqrt{2\nu/a}$	$\sqrt{\nu a/2}$	1	-1
Finite gap, without rotation	L	U_{in}	$U_{\text{in}}L/\nu$	$\hat{\Lambda}_r$
Semi-infinite, rotating disk	$\sqrt{\nu/\Omega}$	$\sqrt{\nu\Omega}$	1	0
Finite gap, rotating disk	L	U_{in}	$U_{\text{in}}L/\nu$	$\hat{\Lambda}_r$

$$\hat{\Lambda}_r \equiv \frac{1}{\hat{r}} \frac{\partial \hat{p}}{\partial \hat{r}} = \frac{\mathcal{L}^2}{\rho_{\text{in}} \mathcal{U}^2} \Lambda_r. \tag{18}$$

The dimensionless temperature and mass fractions are defined as

$$\hat{T} = \frac{T - T_s}{T_{\text{in}} - T_s}, \quad \hat{Y} = \frac{Y - Y_s}{Y_{\text{in}} - Y_s}. \tag{19}$$

2.5. Characteristic scales

In the semi-infinite cases, the characteristic scales are specified in the context of the outer potential flow. For the semi-infinite stagnation flow the scales are

$$\mathcal{L} = \sqrt{\frac{2\nu}{a}}, \quad \mathcal{U} = \sqrt{\frac{\nu a}{2}}. \tag{20}$$

Upon transformation of the governing equations, these scales cause the dimensionless momentum equations to be parameter-free. In other words, as discussed in the following section the Reynolds number is identically unity and the dimensionless pressure-gradient eigenvalue is $\hat{\Lambda}_r \equiv -1$.

In the semi-infinite rotating-disk setting the outer potential flow may be characterized by length and velocity scales that depend on the rotation rate as

$$\mathcal{L} = \sqrt{\frac{\nu}{\Omega}}, \quad \mathcal{U} = \sqrt{\nu\Omega}. \tag{21}$$

As in the semi-infinite stagnation flow case, these characteristic scales cause the dimensionless momentum equations to be parameter-free. The Reynolds number is identically unity and the dimensionless pressure-gradient eigenvalue is $\hat{\Lambda}_r \equiv 0$.

In the finite-gap cases, the characteristic scales are

$$\mathcal{L} = L, \quad \mathcal{U} = U_{\text{in}}, \tag{22}$$

where L is the separation distance between the inlet manifold and the stagnation surface and the U_{in} is a specified inlet velocity.

2.6. Dimensionless equations

The dimensionless governing equations can be summarized as

$$\frac{\mathrm{d}(\hat{\rho}\hat{u})}{\mathrm{d}\hat{z}} + 2\hat{\rho}\hat{V} = 0, \tag{23}$$

$$\hat{\rho}\hat{u}\frac{\mathrm{d}\hat{V}}{\mathrm{d}\hat{z}} + \hat{\rho}\left(\hat{V}^2 - \hat{W}^2\right) = -\hat{\Lambda}_r + \frac{1}{\text{Re}}\frac{\mathrm{d}^2\hat{V}}{\mathrm{d}\hat{z}^2}, \tag{24}$$

$$\hat{\rho}\hat{u}\frac{\mathrm{d}\hat{W}}{\mathrm{d}\hat{z}} + 2\hat{\rho}\hat{V}\hat{W} = \frac{1}{\text{Re}}\frac{\mathrm{d}^2\hat{W}}{\mathrm{d}\hat{z}^2}, \tag{25}$$

$$\hat{\rho}\hat{u}\frac{\mathrm{d}\hat{T}}{\mathrm{d}\hat{z}} = \frac{1}{\text{RePr}}\frac{\mathrm{d}^2\hat{T}}{\mathrm{d}\hat{z}^2}, \tag{26}$$

$$\hat{\rho}\hat{u}\frac{\mathrm{d}\hat{Y}}{\mathrm{d}\hat{z}} = \frac{1}{\text{ReSc}}\frac{\mathrm{d}}{\mathrm{d}\hat{z}}\cdot\left(\hat{\rho}\frac{\mathrm{d}\hat{Y}}{\mathrm{d}\hat{z}}\right) \tag{27}$$

The equation of state can be used to represent the dimensionless density in terms of the dimensionless temperature as

$$\hat{\rho} = \frac{\rho}{\rho_{\text{in}}} = \frac{T_{\text{in}}}{\hat{T}\Delta T + T_s}, \tag{28}$$

where $\Delta T = T_{\text{in}} - T_s$. For the case of an incompressible fluid, the density is assumed to be constant.

The dimensionless groups that appear in the governing equations are the Reynolds, Prandtl, and Schmidt numbers,

$$\text{Re} \equiv \frac{\mathcal{U}\mathcal{L}}{\nu_{\text{in}}} = \frac{\rho_{\text{in}}\mathcal{U}\mathcal{L}}{\mu_{\text{in}}}, \quad \text{Pr} \equiv \frac{\nu_{\text{in}}}{\alpha_{\text{in}}} = \frac{\mu_{\text{in}}c_{p,\text{in}}}{\lambda_{\text{in}}}, \tag{29}$$

$$\text{Sc} \equiv \frac{\mu_{\text{in}}}{\rho_{\text{in}}D_{\text{in}}} = \frac{\nu_{\text{in}}}{D_{\text{in}}}. \tag{30}$$

The transport properties (i.e., dynamic viscosity μ_{in}, kinematic viscosity ν_{in}, heat capacity $c_{p,\text{in}}$, thermal diffusivity α_{in}, and diffusion coefficient D_{in}) are evaluated at the far-field or inlet conditions. The diffusion coefficient D represents the diffusion of the dilute reactive species "A" in a carrier fluid. Although not appearing directly in the governing equations, a rotation Reynolds number is used subsequently,

$$\text{Re}_\Omega \equiv \frac{\rho_{\text{in}}\Omega\mathcal{L}^2}{\mu_{\text{in}}} = \frac{\Omega\mathcal{L}^2}{\nu_{\text{in}}}. \tag{31}$$

2.7. Dimensionless boundary conditions

In dimensionless form, the stagnation-surface boundary conditions ($z = 0$) may be stated as

$$\hat{u} = 0, \quad \hat{V} = 0, \quad \hat{W} = \Omega\frac{\mathcal{L}}{\mathcal{U}}, \quad \hat{T} = 0, \quad \hat{Y} = 0. \tag{32}$$

The stagnation-surface boundary condition for the circumferential velocity may also be written in terms of a ratio of Reynolds numbers as

$$\hat{W} = \frac{\text{Re}_\Omega}{\text{Re}_U}, \tag{33}$$

where the denominator Re_U is the usual Reynolds number based on velocity. Based on their definitions (Eq. (19)), the dimensionless temperature and mass fraction at the surface are $\hat{T} = 0$ and $\hat{Y} = 0$. Although $\hat{Y} = 0$, independent of the surface chemistry, the actual mass fraction is recoverable from the dimensionless solution.

The far-field boundary conditions ($\hat{z} = \hat{z}_{\text{end}}$) are specified in Table 2. The position of $\hat{z}_{\text{end}}$ depends on the flow domain. For the finite-gap subcases $\hat{z}_{\text{end}} = 1$; for the semi-infinite domain $\hat{z}_{\text{end}}$ is chosen to be a value large enough to be well into the inviscid region above the boundary layer.

2.8. Nusselt and Sherwood numbers

The heat flux at the stagnation surface may be evaluated using Fourier's law as

$$q = -\lambda\frac{dT}{dz}. \tag{34}$$

Table 2
Dimensionless boundary conditions at $\hat{z} = \hat{z}_{\text{end}}$.

Geometry	$\hat{u}$	$\hat{V}$	$\hat{W}$	$\hat{T}$	$\hat{Y}$
Semi-infinite, without rotation	–	1	0	1	1
Finite gap, without rotation	1	0	0	1	1
Semi-infinite, rotating disk	–	0	0	1	1
Finite gap, rotating disk	1	0	0	1	1

The heat flux may also be represented in terms of a heat-transfer coefficient in the form of Newton's law of cooling as

$$q = -h(T_{in} - T_s) = -h\Delta T, \tag{35}$$

where $\Delta T = T_{in} - T_s$. Equating these expressions and putting in dimensionless form yields

$$\left.\frac{d\hat{T}}{d\hat{z}}\right)_s = \frac{h\mathcal{L}}{\lambda} \equiv \text{Nu}, \tag{36}$$

where the Nusselt number represents a dimensionless heat-transfer coefficient.

The flux of species A to heterogeneous reaction at the surface may be represented using Fick's law as

$$j_A = -\rho D \frac{dY}{dz}. \tag{37}$$

Alternatively, the surface flux may be expressed as

$$j_A = -h_m \rho (Y_{in} - Y_s) = -\rho h_m \Delta Y, \tag{38}$$

where h_m is a mass-transfer coefficient and $\Delta Y = Y_{in} - Y_s$. Equating the alternative representations of j_A and putting into dimensionless form provides

$$\left.\frac{d\hat{Y}}{d\hat{z}}\right)_s = \frac{h_m \mathcal{L}}{D} \equiv \text{Sh}, \tag{39}$$

where the Sherwood number represents a dimensionless mass-transfer coefficient.

Note that the dimensionless equations and boundary conditions do not depend on the surface reaction rate. However, with a dimensionless solution in hand, the composition at the surface (i.e., Y_s) can be evaluated. Begin by introducing a Damköhler number, which represents a dimensionless ratio of reaction rate and species diffusion,

$$\text{Da} = \frac{k\mathcal{L}}{D}. \tag{40}$$

For gas-surface reactions, Da is bounded as

$$0 \leqslant \text{Da} \leqslant \sqrt{\frac{RT_s}{2\pi W_A}} \frac{\mathcal{L}}{D}. \tag{41}$$

The surface mass balance (i.e., Eqs. (37)–(39)) can be put into dimensionless form as

$$\frac{h_m \mathcal{L}}{D} = \frac{\mathcal{L}}{(Y_{in} - Y_s)} \frac{k}{D} Y_s. \tag{42}$$

Using the definitions of the Sherwood and Damköhler numbers, this relationship can be written as

$$\text{Sh} = \frac{Y_s}{(Y_{in} - Y_s)} \text{Da}. \tag{43}$$

With the Sherwood number being evaluated from the dimensionless solution (Eq. (39)) and the Damköhler number being specified, the surface mass fraction is easily evaluated from Eq. (43) as

$$Y_s = \frac{\text{Sh}}{\text{Da} + \text{Sh}} Y_{in}. \tag{44}$$

By using Y_s in Eq. (11), the species destruction/creation rate $\dot{m}$ can also be recovered from dimensionless solution.

2.9. Rotating-disk inlet velocity

The rotating stagnation surface behaves as a so-called von Kármán pump, where the outer-edge inlet velocity depends upon the rotation rate. Assuming constant properties and a semi-infinite domain, the induced outer-edge axial velocity is

$$u_{in} = -0.88\sqrt{\nu\Omega}, \quad \hat{u}_{in} = -0.88. \tag{45}$$

In the finite gap setting, the stagnation-surface rotation continues to induce an axial velocity. As long as the inlet specified inlet velocity via the manifold meets or exceeds the flow demanded by the disk rotation (i.e., Eq. (45)), the system of equations (Eqs. (23)–(27)) remains valid. However, if the specified inlet velocity is lower than that demanded by the disk rotation, then the analysis here breaks down. Physically, a flow recirculation is induced, which violates the assumptions required to derive the stagnation-flow equations from the full Navier–Stokes equations. If a rotating-disk reactor is designed or operated with "starved" flow, then the models discussed in the present paper are invalid. Full two- or three-dimensional computational fluid dynamics models are required.

2.10. Computational solution

Eqs. (23)–(27) form an ordinary-differential-equation boundary-value problem that may be solved computationally. The computational approach employed here uses a finite-volume discretization on an adaptive mesh network [51,29]. Following discretization of the spatial operators, the resulting system of algebraic equation is solved with a modified Newton algorithm.

2.11. Limitations

Because the overall objective is to derive dimensionless correlations, the foregoing governing equations are based on some significant simplifications. For example, gas-phase chemistry is neglected and the surface chemistry uses a single first-order reaction. The similarity form of the equations themselves can easily accommodate detailed homogeneous and heterogeneous reaction chemistry as well as other physics such as droplet vaporization [29,35,37–39,52,53,19,54]. It is also possible to include high-speed-flow behaviors such as viscous dissipation. However, incorporating such chemical and physical complexities frustrates the ability to correlate results in terms of straightforward relationships among dimensionless parameters.

The present analysis considers only laminar flow. The transition to turbulence would invalidate the laminar-based correlations. In rotating-disk systems turbulent transition is found to occur in the range of

$$\text{Re}_r = \frac{\rho\Omega r^2}{\mu} \approx 2 \times 10^5, \tag{46}$$

where the Reynolds number is based on the disk radius [55,56,32]. The present analysis is based on a Reynolds number in which the length scale is the separation distance between the inlet manifold and the stagnation surface, L. Correlations are presented for Reynolds numbers up to $\text{Re}_L = 10^4$, which would represent a very high-speed flow. Thus, based on a turbulent transition at $\text{Re}_r = 2 \times 10^5$, the present correlations would be valid only up to $r/L = \sqrt{20} \approx 4.5$. Of course, at lower Reynolds numbers the similarity analysis would be valid for much-larger-radius disks.

3. Nusselt number correlations

Nusselt number correlations are first developed for an incompressible fluid (i.e., constant density) with constant properties. In this case, the model is independent of the specific temperatures T_{in} and T_s. In a subsequent section (Section 6) heat and mass transfer correlations are developed for an ideal gas, where the Nusselt and Sherwood numbers have temperature dependencies.

3.1. Semi-infinite domain

Assuming incompressible, constant-property flow, in the semi-infinite setting, the Nusselt number depends on Prandtl number alone. Fig. 2a shows profiles of the dimensionless temperature $\hat{T}$ as a function of dimensionless height above the surface $\hat{z}$ for the semi-infinite stagnation-flow. Fig. 2b shows dimensionless temperature profiles for the semi-infinite rotating-disk. In both cases, the flow is characterized by viscous boundary layer above the stagnation surface and an outer potential flow. The boundary-layer thicknesses decrease as Prandtl number increases. For a given Prandtl number, the boundary layer thickness is greater for the rotating-disk flow that it is for the semi-infinite stagnation flow (note the $\hat{z}$ scale differences between Fig. 2a and b.) The extent of the boundary-layer thickness, and hence the extent of the computational domain, depends on the Prandtl number. For very small values of Pr (e.g., Pr = 0.1), the thermal boundary layer can extend out to $\hat{z} = 25$ or beyond.

Based on solutions such as shown in Fig. 2, the Nusselt number can be evaluated (i.e., Eq. (36)). Fig. 3 shows Nusselt numbers as functions of Prandtl number for both semi-infinite stagnation flow and rotating disk flow. The Nusselt numbers increase with increasing Prandtl number. At a given Pr, the Nu for stagnation-flow is always greater than it is for the rotating disk.

The semi-infinite Nusselt numbers can be fit as functions of Pr in the following form

$$\mathcal{C}_i(x) = A_i x^3 + B_i x^2 + C_i x + D_i, \tag{47}$$

where $x \equiv \log_{10}(\mathrm{Pr})$. The function $\mathcal{C}_i$ represents either $\mathcal{S}_{si}$ for the semi-infinite flow or $\mathcal{R}_{si}$ for the rotating disk. That is,

$$\mathrm{Nu(Pr)} = \mathcal{S}_{si}(x), \quad \mathrm{Nu(Pr)} = \mathcal{R}_{si}(x), \tag{48}$$

for stagnation flow and rotating disk, respectively, using the polynomial form in Eq. (47). Table 3 lists the coefficients.

Prandtl numbers for low-pressure gases are always around $\mathrm{Pr} \approx 0.7$. Prandtl numbers for liquids (e.g., aqueous mixtures or light hydrocarbons) are typically much larger. The present analysis considers the range $0.5 \leqslant \mathrm{Pr} \leqslant 100$. It is worth noting that in both the semi-infinite stagnation flow and rotating disk subcases, the Nu-scaling increases *approximately* as $\mathrm{Pr}^{1/3}$, which is typical of laminar flow Nusselt-number correlations.

3.2. Finite-gap domain

Fig. 4 shows dimensionless temperature profiles for finite-gap stagnation flow. Fig. 4a shows Reynolds number dependence with fixed Pr = 1. Above about $\mathrm{Re}_U = 5$, the thermal boundary layer thickness decreases as $\mathrm{Re}_U^{-1/2}$. This behavior arises because of the
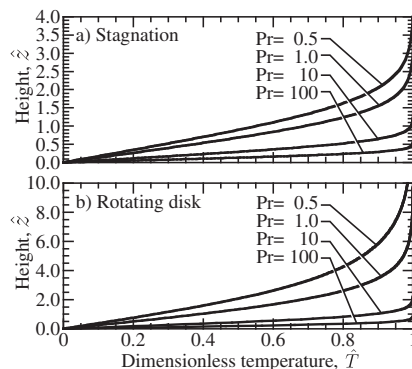

Fig. 2. Dimensionless temperature profiles for a range of Prandtl numbers. (a) Semi-infinite stagnation flow, and (b) Semi-infinite rotating disk.
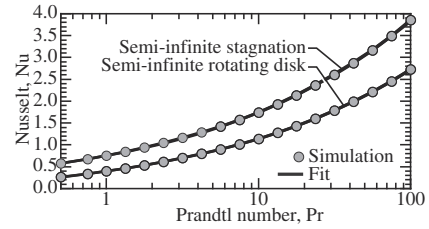

Fig. 3. Correlation of Nusselt number as function of Prandtl number for semi-infinite stagnation flow and rotating disk flow. The points are from individual simulations and the solid curves represent the polynomial fits.

Table 3
Coefficients in fits of cubic polynomials in $x \equiv \log_{10}(\mathrm{Pr})$.

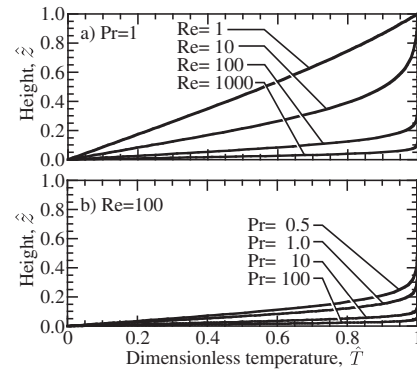| Coefficient	$\mathcal{R}_{si}$	$\mathcal{S}_{si}$	ξ
A_i (x^3 term)	0.09728	0.09456	0.01107
B_i (x^2 term)	0.13265	0.26266	−0.07089
C_i (x^1 term)	0.50582	0.63615	0.21017
D_i (x^0 term)	0.40214	0.75253	0.27645

Fig. 4. Dimensionless temperature profiles for finite-gap stagnation flow. (a) Profiles for different values of Reynolds number and Pr = 1; (b) Profiles for different values of Prandtl number and $\mathrm{Re}_U = 100$.

essentially inviscid flow between the inlet manifold and viscous boundary layer near the surface. As the Reynolds number increases, the outer viscous layer becomes thinner and fills less of the gap. However, as the Reynolds number decreases to below around 10, the viscous layer fills the entire gap. For sufficiently low Reynolds number the fluid flow becomes negligible and the heat transfer is dominated by thermal conduction; in that limit the Nusselt number approaches unity.

Fig. 4b shows Prandtl number dependence with fixed $\mathrm{Re}_U = 100$. The trends are similar to those for the semi-infinite cases (cf., Fig. 2). At high Pr, the viscous boundary-layer thickness is much smaller than the gap. In these cases, the Nusselt-number correlation is similar to that found for the semi-infinite flow.

Fig. 5 shows Nusselt number (symbols) as a function of Re_U for four values of Pr. For $\mathrm{Re}_U \gtrsim 10$, the Nusselt number increases as $\mathrm{Nu} \propto \sqrt{\mathrm{Re}_U}$. At low Re_U where the boundary layer fills the gap (cf., Fig. 4a), the Nu dependence deviates from the square-root dependence. At low Re_U, Nu approaches a constant value of unity, indicating dominantly diffusion with negligible fluid flow.

As long as the boundary layer does not fill the gap, the Nusselt number for finite-gap stagnation flow, is well represented by the correlation

$$\mathrm{Nu} = \mathcal{S}_{si}(\mathrm{Pr}) \times \mathrm{Re}_U^{1/2}. \tag{49}$$
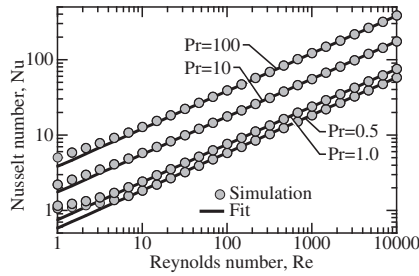
Fig. 5. Correlation of Nusselt number with Reynolds and Prandtl numbers for finite-gap stagnation flow. Markers represent numerical calculations; solid curves are evaluated using the expression in Eq. (49).

Fig. 5 shows this correlation as solid lines for different values of Pr.

It is interesting to realize that the Pr-dependence derived from the *semi-infinite* stagnation flow Nusselt-number correlation (i.e., $\mathcal{S}_{si}$) carried over directly to the *finite-gap* correlation. This result is consistent with the notion that the flow in the finite-gap case can be described as an inner viscous boundary layer below an outer inviscid potential flow.

4. Sherwood number correlation

The Sherwood number is used to correlate the mass-transfer coefficient at the stagnation surface. For an incompressible fluid, the Nusselt- and Sherwood-number correlations are essentially identical, with the Prandtl and Schmidt numbers playing analogous roles. This behavior is the result of Eqs. (26) and (27) being completely analogous.

4.1. Semi-infinite domain

Fig. 6 shows dimensionless mass fractions as functions of dimensionless height for semi-infinite stagnation and rotating-disk flow. Comparisons with Fig. 2 show identical profiles, but with Sc replacing Pr and $\hat{Y}$ replacing $\hat{T}$. Consequently, the Sherwood number correlations follow the same function as the Nusselt number (i.e., Eq. (47)), but with Schmidt number taking the place of Prandtl number. That is,

$$\mathrm{Sh}(\mathrm{Sc}) = \mathcal{S}_{si}(x), \quad \mathrm{Sh}(\mathrm{Sc}) = \mathcal{R}_{si}(x), \tag{50}$$

for stagnation flow and rotating disk, respectively. In evaluating Eq. (47), $x = \log_{10}(\mathrm{Sc})$ and the coefficients are listed in Table 3. The behavior is the same as shown in Fig. 3, but with Sh taking the place of Nu and Sc taking the place of Pr.
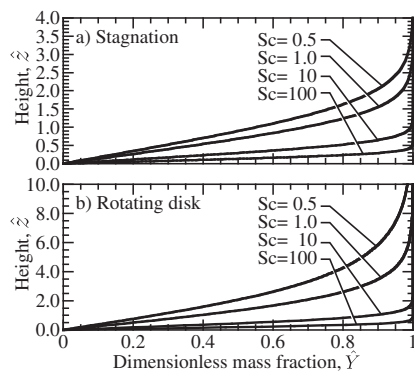
Fig. 6. Dimensionless species mass-fraction profiles for different values of Schmidt number (a) for semi-infinite stagnation flow, and (b) for the semi-infinite rotating disk.

4.2. Finite-gap stagnation flow

As in the case of semi-infinite flow, the finite-gap behavior for dimensionless mass fraction profiles and Sherwood-number correlations is completely analogous with the behavior for dimensionless temperature profiles and Nusselt-number correlations. The dimensionless mass fractions are analogous to the temperature profiles shown in Fig. 4, but with Sc taking the place of Pr. The Sherwood number correlations are the same as shown in Fig. 4, but with Sh replacing Nu and with Sc replacing Pr.

5. Composite Reynolds number

Practical rotating-disk reactors such as for chemical vapor deposition introduce the reactive fluid through a manifold such as shown in Fig. 1. In this finite-gap case, the flow may be a combination of ideal stagnation-flow and rotating-disk flow. Thus, correlations are needed that accommodate the combination of stagnation-surface rotation and imposed manifold flow. The present analysis introduces a "composite Reynolds number" as the basis for the correlations [57].

For the semi-infinite rotating disk, the Nusselt number correlation is represented as

$$\mathrm{Nu} = \mathcal{R}_{si}(\mathrm{Pr}) = \frac{h\mathcal{L}}{\lambda} = \frac{h}{\lambda}\sqrt{\frac{\nu}{\Omega}}, \tag{51}$$

where the expression for the characteristic length scale $\mathcal{L}$ (Table 1) is explicitly substituted. The product of the semi-infinite Nusselt correlation and the square root of the rotational Reynolds number (Eq. (31)) yields

$$\mathcal{R}_{si}\sqrt{\mathrm{Re}_\Omega} = \frac{h}{\lambda}\sqrt{\frac{\nu}{\Omega}} \times \sqrt{\frac{\Omega}{\nu}}L = \frac{hL}{\lambda} \equiv \mathrm{Nu}. \tag{52}$$

In the limit that the finite-gap height L is much greater than the characteristic boundary-layer thickness $\mathcal{L}$ for the semi-infinite rotating disk, the Nu should be expected scale as the square-root of Re_Ω. It was previously shown that the Nusselt number for finite-gap stagnation flow may be correlated as

$$\mathrm{Nu} = \mathcal{S}_{si}\sqrt{\mathrm{Re}_U}. \tag{53}$$

As long as there is a region of inviscid flow in the region above the viscous boundary layer, a composite Reynolds number can be defined that correlates the Nusselt number in a finite stagnation-flow gap, including the effect of rotation. The proposed composite Reynolds number is

$$\mathrm{Re}_c = \sqrt{(\xi\mathrm{Re}_\Omega)^2 + (\mathrm{Re}_U)^2}, \tag{54}$$

where $\xi(\mathrm{Pr})$ is a function of Prandtl number as

$$\xi(\mathrm{Pr}) = \left(\frac{\mathcal{R}_{si}}{\mathcal{S}_{si}}\right)^2. \tag{55}$$

The proposed Nusselt-number correlation is

$$\mathrm{Nu} = \mathcal{S}_{si}\sqrt{\mathrm{Re}_c}. \tag{56}$$

It is evident by inspection that this correlation satisfies both Eqs. (52) and (53) in the limits that there is either no surface rotation or pure semi-infinite rotating-disk flow. The factor $\xi(\mathrm{Pr})$ in Eq. (54) is grounded in satisfying the limiting cases. Increasing either of the Reynolds numbers has the effect of increasing the flow rate, thinning the boundary layer, and thus increasing the surface heat transfer. However, the magnitudes of the two Reynolds numbers cannot be compared directly to each other to determine their relative effects on boundary-layer behavior. For example, when $\mathrm{Pr} = 0.7$, Re_Ω needs to be roughly four times greater that Re_U to

achieve the same heat transfer. Heat is transferred through the viscous boundary layer and equivalent boundary-layer behavior can be achieved either through varying rotation rate or increasing the forced velocity at the inlet. The correlation provides the quantitative relationship of the overall results for differing modes of establishing the boundary layer. Even when the boundary layer behaviors are comparable in overall result, the outer flows that support them can be quite different.

The Prandtl-number dependence of the factor ξ (Eq. (55)) can be represented by a cubic polynomial in $x \equiv \log_{10}(\mathrm{Pr})$ as

$$\xi(x) = A_i x^3 + B_i x^2 + C_i x + D_i. \tag{57}$$

Based on the computational solutions, the factor ξ was evaluated numerically for Prandtl numbers ranging from 0.5 to 100 and the results are plotted in Fig. 7 as the marker symbols. Table 3 lists the polynomial coefficients $A_i - D_i$ for the fit to ξ. The fit is plotted as a solid line.

The results present to this point have considered incompressible fluids with constant properties. Consequently, as discussed in Section 4, under these assumptions the Sherwood number is numerically equivalent to the Nusselt number. Therefore, the proposed Sh correlation is

$$\mathrm{Sh} = \mathcal{S}_{\mathrm{si}} \sqrt{\mathrm{Re}_c}. \tag{58}$$

Fig. 8 shows dimensionless temperature profiles for mixed stagnation/rotating-disk flow, holding Re_c fixed, but with greatly different combinations of Re_Ω and Re_U. Fig. 8a fixes $\mathrm{Re}_c = 100$ and shows dimensionless temperature profiles for the four different Reynolds numbers. The results are sufficiently similar as to be nearly indistinguishable in the plot. The boundary-layer thickness in each example is on the order of $\hat{z} = 0.25$, so the necessary requirement that it be small compared to the gap in order for the composite Reynolds number correlation to be valid is certainly satisfied. The calculated Nusselt numbers for the four examples plotted are within 1% of one another.

Fig. 8b is similar to Fig. 8a, but with $\mathrm{Re}_c = 10$. Although the profiles are indeed very close at the surface, larger deviations are more evident away from the surface. The deviations are the result of the thermal boundary layer thickness being comparable to the gap dimension. Thus, $\mathrm{Re}_c \approx 10$ was found to be the lower limit for the accuracy of the composite Reynolds number correlation. The actual Nusselt numbers differed by about 4% for the four cases shown in Fig. 8b.

Using a widely ranging combination of Re_Ω and Re_U), Fig. 9 compares Nusselt numbers evaluated directly from the computational solutions with the composite Reynolds number correlation. The square-root dependence on composite Reynolds number is consistent with the results shown in Fig. 5. As illustrated by the dimensionless temperature profiles in Fig. 8b the square-root dependence starts to breakdown below about $\mathrm{Re}_c \approx 10$ (lower values were not plotted in Fig. 9). The correlation (Eq. (56)) clearly
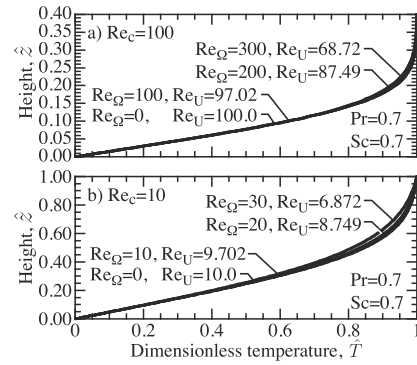
Fig. 8. Dimensionless temperature profiles for the finite-gap flow subcase (Sc = Pr = 0.7) for combinations of Re_Ω and Re_U such that (a) $\mathrm{Re}_c = 100$, and (b) $\mathrm{Re}_c = 10$.
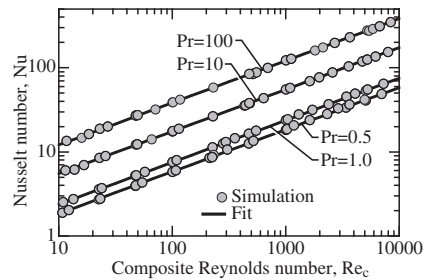
Fig. 9. Correlation of finite-gap Nusselt number with the composite Reynolds number for different values of Prandtl number. Markers represent computational simulations for many different combinations of Re_Ω and Re_U to comprise the resultant Re_c. The solid curves represent the composite Reynolds number correlation.

provides an excellent representation of the results over wide ranges of flow conditions.

As noted previously, assuming an incompressible fluid with constant properties, the dimensionless energy and species equations (Eqs. (26) and (27)) are directly analogous. Thus, the Sherwood numbers are the same as the Nusselt numbers, but with Sc replacing Pr.

6. Ideal gas correlations

In previous sections, Nusselt and Sherwood correlations were developed for incompressible fluids and a wide range of Prandtl and Schmidt numbers. However, many practical applications (e.g., chemical vapor deposition) involve gases and large temperature variations. The present section extends the analysis to include ideal gases, where the temperature variations play a significant role in affecting the density and hence the flow fields. The present analysis continues to assume constant Prandtl and Schmidt numbers. For ideal gases, the Prandtl and Schmidt numbers do remain essentially constant, even though the contributing properties (i.e., viscosity, thermal conductivity, and diffusion coefficients) depend on temperature. The following analysis assumes Pr = Sc = 0.7.

6.1. Stagnation-flow Nusselt number

Fig. 10 shows profiles of dimensionless temperature, mass fraction, and density in finite-gap stagnation flow with different surface temperatures. In all cases, the inlet temperature is $T_{\mathrm{in}} = 300$ K and $\mathrm{Re}_U = 100$; however, the surface temperatures vary between $600 \leqslant T_s \leqslant 1800$ K. Because the density depends upon
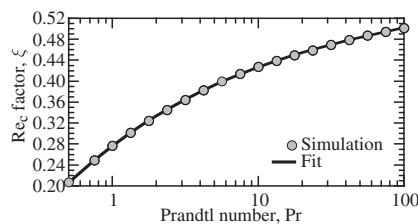

Fig. 7. Multiplicative factor ξ in the evaluation of the composite Reynolds number. Marker symbols represent simulated values of the ξ using Eq. (55). The solid curve is the cubic-polynomial fit in Eq. (57).
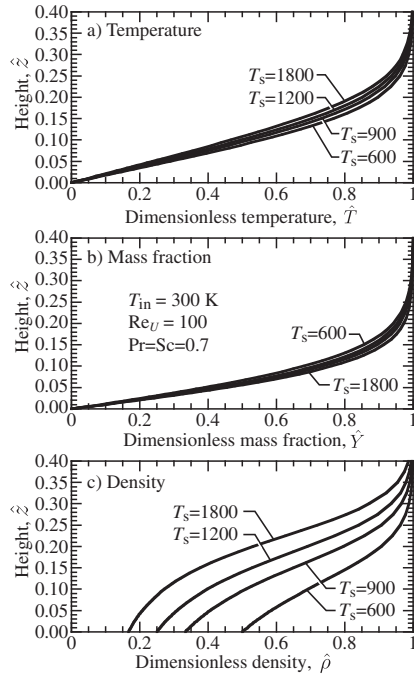
Fig. 10. Calculated profiles of (a) dimensionless temperature, (b) dimensionless mass fraction, and (c) dimensionless density for finite-gap stagnation flow. T_{in} is fixed at 300 K and the surface temperature varied, with T_s = 600, 1200, and 1800 K. In all cases Pr = Sc = 0.7 and Re_U = 100.

temperature (Eq. (28)), all the conservation equations (Eqs. (23)–(27)) must depend on the temperature variations via the density. However, despite the large variations in dimensionless density (Fig. 10c), the variations in dimensionless temperature and mass-fraction profiles are relatively weak (Figs. 10a,b).

The dimensionless temperature and mass-fraction profiles are quite similar, but certainly not the same. The reason is related to the influence of the density. The dimensionless species equation (Eq. (27)) involves density within the diffusion term but the dimensionless energy equation (Eq. (26)) does not. The thermal boundary layer is thicker than the species boundary layer. The thermal boundary-layer thickness increases as the surface temperature increases. The species boundary layer shows the opposite behavior.

Straightforward rearrangement of Eq. (28) shows that the dimensionless density depends on the ratio of surface and inlet temperatures,

$$\Theta \equiv \frac{T_s}{T_{in}}. \tag{59}$$

That is,

$$\hat{\rho} = \frac{1}{\hat{T}(1 - \Theta) + \Theta}. \tag{60}$$

The temperature variations affect the gradients at the surface, and hence the Nusselt and Sherwood numbers. As T_s increases from 600 to 1800 K the Nusselt number decreases by about 20%, but the Sherwood increases by about 20%.

Fig. 11 shows calculated Nusselt numbers as functions of T_s/T_{in} for several inlet Reynolds numbers. These results were evaluated from solutions using T_{in} = 300 K, but varying $300 \leqslant T_s \leqslant 1500$ K (i.e., $1 \leqslant \Theta \leqslant 5$). The Nusselt number decreases with increasing temperature ratio Θ, and for $Re_U > 10$ the Nusselt number can be represented as

$$\text{Nu} = \mathcal{S}_{si} \sqrt{Re_U} \Theta^{-n}, \tag{61}$$
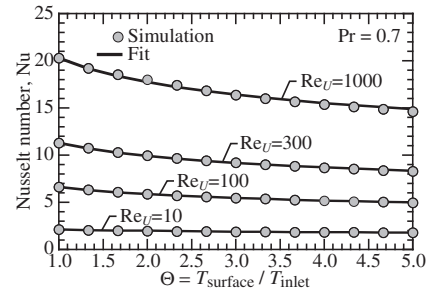
Fig. 11. Finite-gap stagnation flow Nusselt number as function of Θ for different Reynolds numbers. Symbols indicate calculated values of Nu and solid-curves are the correlation expression (Eq. (61)).

with

$$n = 0.0066x^3 - 0.0653x^2 + 0.2244x - 0.0647, \tag{62}$$

and $x = \log_{10} Re_U$. The factor $\mathcal{S}_{si}\sqrt{Re_U}$ represents the Reynolds number functional dependence at $\Theta = 1$. For the ideal gas case considered in this section, $\mathcal{S}_{si}(\text{Pr} = 0.7) = 0.66$. The exponent n represents the Θ dependence (Fig. 11). The polynomial fit for n is valid in the range $10 \leqslant Re_U \leqslant 10,000$. Fig. 11 shows the modeled results as points and fits (i.e., Eq. (61)) as solid lines.

Fig. 12 shows the dependence of Nu on Reynolds number ($Re_U > 10$) for three values of Θ. The $\Theta = 1$ line corresponds to the isothermal finite-gap stagnation flow discussed in Section 3.2. The isothermal Nusselt number is very well represented by a square-root dependence on Reynolds number (Eq. (49)). For $Re_U \gtrsim 100$, Fig. 12 shows that all the lines are parallel with square-root dependence. However, as noted in Fig. 5, the square-root dependence breaks down at low Re as the boundary layer fills the gap. At $\Theta = 5$, Fig. 12 shows that for $Re_U \lesssim 50$ the slope is reduced noticably below the square-root dependence. For example, at $\Theta = 5$ and $Re_U = 10$, the Re dependence decreases to approximately $Re_U^{0.42}$.

6.2. Stagnation flow Sherwood number

Fig. 13 shows Sherwood numbers as functions of $\Theta = T_s/T_{in}$ for several inlet Reynolds numbers. These results were evaluated from solutions using T_{in} = 300 K, but varying $1 \leqslant \Theta \leqslant 5$. The Sherwood numbers increase with the temperature ratio Θ (opposite from the Nusselt number trend) and approach asymptotes at large Θ. The Sherwood-number behavior can be represented as
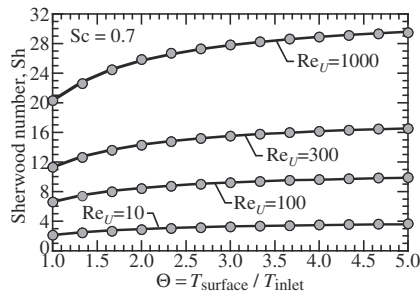
$$\text{Sh} = \mathcal{S}_{si} \sqrt{Re_U} \exp\left(c\frac{\Theta - 1}{\Theta}\right), \tag{63}$$

with

$$c = -0.0144x^3 + 0.1429x^2 - 0.4812x + 1.0124, \tag{64}$$
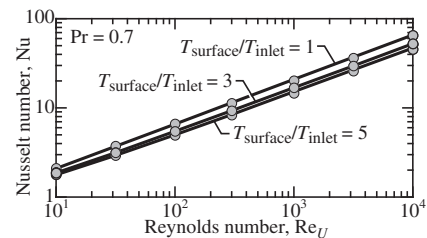
Fig. 12. Finite-gap stagnation flow Nusselt number at Pr = 0.7 as a function of Reynolds number for three values of $\Theta = T_s/T_{in}$. Symbols indicate calculated values of Nu and solid-curves are the correlation expression (Eq. (61)).

Fig. 13. Finite-gap stagnation flow Sherwood number as a function of Θ for different values of the Reynolds number. In all cases, $Sc = 0.7$. The symbols indicate calculated values of Sh and solid lines are the correlation expression (Eq. (63)).
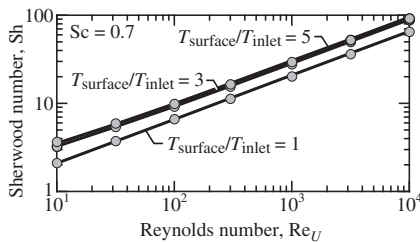
Fig. 14. Finite-gap stagnation flow Sherwood number as a function of Reynolds number, for three different values of $\Theta = T_s/T_{in}$. The symbols indicate calculated values of Sh and solid lines are the correlation expression (Eq. (63)).

and $x = \log_{10} Re_U$. The polynominal fit for c is valid in the range $10 \leqslant Re_U \leqslant 10,000$.

Fig. 14 is analogous to Fig. 12, showing the Θ dependence for Sherwood number. At high Θ the boundary layer fills the gap at lower values of Re_U, thus reducing the Re-number dependence below the square-root behavior at high Reynolds number.

7. Summary

Variants of ideal stagnation flow play important roles in technological applications, such as chemical vapor deposition for fabricating thin-film semiconductor devices. Reactors are developed to realize the surface-flux uniformity associated with ideal stagnation flow. The present paper addresses four different realizations of ideal stagnation flow – semi-infinite stagnation flow, finite-gap stagnation flow, semi-infinite rotating disk flow, and finite-gap rotating disk flow. The underpinning theory for each of these flows has been well known for nearly a century. However, the literature generally treats them as being fundamentally different. This paper presents an analysis that unifies the treatment of these flows. The unified theory is manifested as an ordinary-differential-equation boundary-value problem that can be solved computationally.

Based on solutions of the unified problem, the paper develops general correlations for Nusselt and Sherwood numbers over wide ranges of operating conditions. The correlations can be used to evaluate heat and mass transfer at the stagnation surface.

Acknowledgements

References

[1] G.S. Tompa, P.A. Zawadzki, K. Moy, M. McKee, A.G. Thompson, A.I. Gurary, E. Wolak, P. Esherick, W.G. Breiland, G.H. Evans, N. Bulitka, J. Hennessy, C.J.L. Moore, Design and operating characteristics of a metalorganic vapor phase epitaxy production scale, vertical, high speed, rotating disk reactor, J. Cryst. Growth 145 (1) (1994) 655–661.

[2] R. Walker, A.I. Gurary, C. Yuan, P. Zawadzki, K. Moy, T. Salagaj, A.G. Thompson, W.J. Krolla, R.A. Stall, N.E. Schumaker, Novel high temperature metal organic chemical vapor deposition vertical rotating-disk reactor with multizone heating for GaN and related materials, Mater. Sci. Eng. B 35 (1) (1995) 97–101.

[3] A.G. Thompson, R.A. Stall, P. Zawadzki, G.H. Evans, The scaling of CVD rotating disk reactors to large sizes and comparison with theory, J. Electron. Mater. 25 (9) (1996) 1487–1494.

[4] E.J. Thrush, A.R. Boyd. Close-coupled showerhead MOCVD technology for the epitaxy of GaN and related materials. III-Nitride: Semiconductor Materials, 2006. p. 73.

[5] M. Dauelsberg, C. Martin, H. Protzmann, A.R. Boyd, E.J. Thrush, J. Käppeler, M. Heuken, R.A. Talalaev, E.V. Yakovlev, A.V. Kondratyev, Modeling and process design of III-nitride MOVPE at near-atmospheric pressure in close coupled showerhead and planetary reactors, J. Cryst. Growth 298 (2007) 418–424.

[6] J. Newman, K.E. Thomas-Alyea, Electrochemical Systems, John Wiley & Sons, 2012.

[7] A.J. Bard, L.R. Faulkner, Electrochemical Methods: Fundamentals and Applications, Wiley, New York, 2001.

[8] F. Opekar, P. Beran, Rotating disk electrodes, J. Electroanal. Chem. Interface Electrochem. 69 (1) (1976) 1–105.

[9] J.A. Koutecky, V.G. Levich, The use of a rotating disk electrode in the studies of electrochemical kinetics and electrolytic processes, Zh. Fiz. Khim. 32 (1958) 1565–1575.

[10] D. Jahn, W. Vielstich, Rates of electrode processes by the rotating disk method, J. Electrochem. Soc. 109 (9) (1962) 849–852.

[11] P. Ho, M.E. Coltrin, W.G. Breiland, Laser-induced fluorescence measurements and kinetic analysis of Si atom formation in a rotating disk chemical vapor deposition reactor, J. Phys. Chem. 98 (40) (1994) 10138–10147.

[12] H.A. Gasteiger, N.M. Markovic, P.N. Ross Jr., H₂ and co electrooxidation on well-characterized Pt, Ru, and Pt-Ru. 1. Rotating disk electrode studies of the pure gases including temperature effects, J. Phys. Chem. 99 (20) (1995) 8290–8301.

[13] O. Deutschmann, R. Schmidt, F. Behrendt, J. Warnatz, Numerical modeling of catalytic ignition, Proc. Combust. Inst. 26 (1996) 1747–1754.

[14] T.J. Schmidt, H.A. Gasteiger, G.D. Stäb, P.M. Urban, D.M. Kolb, R.J. Behm, Characterization of high-surface-area electrocatalysts using a rotating disk electrode configuration, J. Electrochem. Soc. 145 (7) (1998) 2354–2358.

[15] O. Deutschmann, L.I. Maier, U. Riedel, A.H. Stroeman, R.W. Dibble, Hydrogen assisted catalytic combustion of methane on platinum, Catal. Today 59 (1) (2000) 141–150.

[16] O. Bautista, F. Mendez, C. Trevino, Theoretical analysis of the direct decomposition of methane gas in a laminar stagnation-point flow: CO₂-free production of hydrogen, Int. J. Hydrogen Energy 33 (24) (2008) 7419–7426.

[17] O.N. Sara, J. Erkmen, S. Yapici, M. Copur, Electrochemical mass transfer between an impinging jet and a rotating disk in a confined system, Int. Commun. Heat Mass Transfer 35 (3) (2008) 289–298.

[18] Y.H. Liu, L.W. Tseng, C.Y. Huang, K.L. Lin, C.C. Chen, Particle image velocimetry measurement of jet impingement in a cylindrical chamber with a heated rotating disk, Int. J. Heat Mass Transfer 65 (2013) 339–347.

[19] C. Karakaya, O. Deutschmann, Kinetics of hydrogen oxidation on Rh/Al₂O₃ catalysts studied in a stagnation-flow reactor, Chem. Eng. Sci. 89 (2013) 171–184.

[20] H. Karadeniz, C. Karakaya, S. Tischer, O. Deutschmann, Numerical modeling of stagnation-flows on porous catalytic surfaces: CO oxidation on Rh/Al–2O₃, Chem. Eng. Sci. 104 (2013) 899–907.

[21] G.D. Wehinger, T. Eppinger, M. Kraume, Fluidic effects on kinetic parameter estimation in lab-scale catalysis testing – A critical evaluation based on computational fluid dynamics, Chem. Eng. Sci. 111 (2014) 220–230.

[22] B. Mitrovic, A. Gurary, L. Kadinski, On the flow stability in vertical rotating disc MOCVD reactors under a wide range of process parameters, J. Cryst. Growth 287 (2) (2006) 656–663.

[23] B. Mitrovic, A. Parekh, J. Ramer, V. Merai, E.A. Armour, L. Kadinski, A. Gurary, Reactor design optimization based on 3D modeling of nitrides deposition in MOCVD vertical rotating disc reactors, J. Cryst. Growth 289 (2) (2006) 708–714.

[24] B. Mitrovic, A. Gurary, W. Quinn, Process conditions optimization for the maximum deposition rate and uniformity in vertical rotating disc MOCVD reactors based on CFD modeling, J. Cryst. Growth 303 (1) (2007) 323–329.

[25] C.R. Kleijn, R. Dorsman, K.J. Kuijlaars, M. Okkerse, H. Van Santen, Multi-scale modeling of chemical vapor deposition processes for thin film technology, J. Cryst. Growth 303 (1) (2007) 362–380.

[26] K. Hiemenz, Die grenzschict an einem in den gleichförmigen flüssigkeitsstrom eingetauchten geraden kreiszylinder, Dinglers Polytech. J. 326 (1911) 321–410.

[27] F. Homann, Der einfluss grosser zähigkeit bei der strömung um den zylinder und um die kugel, Z. Angew. Math. Mec. 16 (1936) 153–164.

[28] T. von Kármán, Über laminare und turbulente reibung, Z. Angew. Math. Mech. 1 (1921) 233–252.

[29] R.J. Kee, M.E. Coltrin, P. Glarborg, Chemically Reacting Flow: Theory and Practice, Wiley, Hoboken, NJ, 2003.

[30] F.M. White, Viscous Fluid Flow, McGraw-Hill, New York, 2011.

[31] H. Schlichting, K. Gersten, Boundary-Layer Theory, McGraw-Hill, New York, 2003.

[32] I.V. Shevchuk, Modelling of Convective Heat and Mass Transfer in Rotating Flows, Springer, New York, 2015.

[33] T.W. Chapman, G.L. Bauer, Stagnation-point viscous flow of an incompressible fluid between porous plates with uniform blowing, Appl. Sci. Res. 31 (1975) 223–239.

[34] K. Sheshadri, F.A. Williams, Laminar flow between parallel plates with injection of a reactant at high Reynolds number, Int. J. Heat Mass Transfer 21 (1978) 251–253.

[35] R.J. Kee, J.A. Miller, G.H. Evans, G. Dixon-Lewis, A computational model of the structure and extinction of strained, opposed-flow, premixed, methane-air flames, Proc. Combust. Inst. 22 (1988) 1479–1493.

[36] G. Evans, R. Greif, Forced flow near a heated rotating disk: a similarity solution, Numer. Heat Transfer 14 (3) (1988) 373–387.

[37] M.E. Coltrin, R.J. Kee, G.H. Evans, E. Meeks, F.M. Rupley, J.F. Grcar, SPIN: a Fortran program for modeling one-dimensional rotating-disk/stagnation-flow chemical vapor deposition reactors, Technical Report SAND91-8003, Sandia National Laboratories, 1991.

[38] M.E. Coltrin, R.J. Kee, G.H. Evans, A mathematical model of the fluid mechanics and gas-phase chemistry in a rotating disk chemical vapor deposition reactor, J. Electrochem. Soc. 136 (3) (1989) 819–829.

[39] J. Warnatz, M.D. Allendorf, R.J. Kee, M.E. Coltrin, A model of elementary chemistry and fluid mechanics in the combustion of hydrogen on platinum surfaces, Combust. Flame 96 (1994) 393–406.

[40] A.C. Riddiford, The rotating disk system, Adv. Electrochem. Electrochem. Eng. 4 (1966) 47–116.

[41] G. Evans, R. Greif, A numerical model of the flow and heat-transfer in a rotating-disk chemical vapor deposition reactor, J. Heat Transfer 109 (4) (1987) 928–935.

[42] G. Evans, R. Greif, Effects of boundary conditions on the flow and heat transfer in a rotating-disk chemical vapor deposition reactor, Numer. Heat Transfer 12 (2) (1987) 243–252.

[43] W.G. Breiland, G.H. Evans, Design and verification of nearly ideal flow and heat transfer in a rotating disk chemical vapor deposition reactor, J. Electrochem. Soc. 138 (6) (1991) 1806–1816.

[44] K.F. McCarty, E. Meeks, R.J. Kee, A.E. Lutz, Scaleable stagnation-flow reactors for uniform materials deposition: application to combustion synthesis of diamond, Appl. Phys. Lett. 63 (11) (1993) 1498–1500.

[45] W.S. Winters, G.H. Evans, R. Greif, Mixed binary convection in a rotating disk chemical vapor deposition reactor, Int. J. Heat Mass Transfer 40 (3) (1997) 737–744.

[46] C.R. Kleijn, Computational modeling of transport phenomena and detailed chemistry in chemical vapor deposition–A benchmark solution, Thin Solid Films 365 (2000) 294–306.

[47] Helmar van Santen, Chris R. Kleijn, Harry E.A. van den Akker, On multiple stability of mixed-convection flows in a chemical vapor deposition reactor, Int. J. Heat Mass Transfer 44 (3) (2001) 659–672.

[48] G. Luo, S.P. Vanka, N. Glumac, Fluid flow and transport processes in a large area atmospheric pressure stagnation flow {CVD} reactor for deposition of thin films, Int. J. Heat Mass Transfer 47 (23) (2004) 4979–4994.

[49] M.-H. Liao, C.-H. Chen, S.-C. Kao, The novel chamber hardware design to improve the thin film deposition quality in both 12 (300 mm) and 18 (450 mm) wafers with the development of 3d full chamber modeling and experimental visual technique, Int. J. Heat Mass Transfer 67 (2013) 393–397.

[50] C.L. Tien, J. Tsuji, Heat transfer by laminar forced flow against a non-isothermal rotating disk, Int. J. Heat Mass Transfer 7 (2) (1964) 247–252.

[51] J.F. Grcar, R.J. Kee, M.D. Smooke, J.A. Miller, A hybrid Newton/time-integration procedure for the solution of steady, laminar, one-dimensional premixed flames, Proc. Combust. Inst. 21 (1986) 1773–1782.

[52] N.E. McGuire, N.P. Sullivan, O. Deutschmann, H. Zhu, R.J. Kee, Dry reforming of methane in a stagnation-flow reactor using Rh supported on strontium-substituted hexaaluminate, Appl. Catal. A 394 (2011) 257–265.

[53] H. Zhu, R.J. Kee, L. Chen, J. Cao, M. Xu, Y. Zhang, Vaporisation characteristics of methanol, ethanol and heptane droplets in opposed stagnation flow at low temperature and pressure, Combust. Theory Model. 16 (2012) 715–735.

[54] H. Zhu, Y. Zhang, M. Xu, R.J. Kee, Droplet vaporization characteristics of multicomponent mixtures of methanol and gasoline surrogate in opposed stagnation flows, Proc. Combust. Inst. 34 (2013) 1545–1552.

[55] D.-T. Chin, M. Litt, An electrochemical study of flow instability on a rotating disk, J. Fluid Mech. 54 (1972) 613–625.

[56] S. Harmand, J. Pellé, S. Poncet, I.V. Shevchuk, Review of fluid flow and convective heat transfer within rotating disk cavities with impinging jet, Int. J. Therm. Sci. 67 (2013) 1–30.

[57] T. Astarita, G. Cardone, Convective heat transfer on a rotating disk with a centred impinging round jet, Int. J. Heat. Mass Transfer 51 (7–8) (2008) 1562–1572.